Nanoscale

Accepted Manuscript

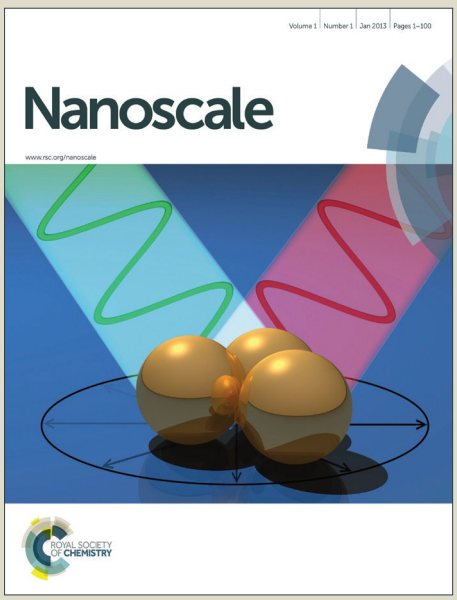

ROYAL SOCIETY OF CHEMISTRY

www.rsc.org/nanoscale

Nanoscale

ARTICLE

Tuneable 2D self-assembly of plasmonic nanoparticles at liquid | liquid interfaces

Received 00th January 20xx,
Accepted 00th January 20xx

DOI: 10.1039/x0xx00000x

www.rsc.org/

Leonora Velleman,[a] Debabrata Sikdar,[a] Vladimir A. Turek,[a] Anthony R. Kucernak,[a] Steve J. Roser,[b]* Alexei A. Kornyshev,[a]* and Joshua B. Edel,[a]*

Understanding the structure and assembly of nanoparticles at liquid | liquid interfaces is paramount to their integration into devices for sensing, catalysis, electronics and optics. However, many difficulties arise when attempting to resolve the structure of such interfacial assemblies. In this article we use a combination of X-ray diffraction and optical reflectance to determine the structural arrangement and plasmon coupling between 12.8 nm diameter gold nanoparticles assembled at a water | 1,2-dichloroethane interface. The liquid | liquid interface provides a molecularly flat and defect-correcting platform for nanoparticles to self-assemble. The amount of nanoparticles assembling at the interface can be controlled via the concentration of electrolyte within either the aqueous or organic phase. At higher electrolyte concentration more nanoparticles can settle at the liquid | liquid interface resulting in a decrease in nanoparticle spacing as observed from X-ray diffraction experiments. The coupling of plasmons between the nanoparticles as they come closer together is observed by a red-shift in the optical reflectance spectra. The optical reflectance and the X-ray diffraction data are combined to introduce a new 'plasmon ruler'. This allows extraction of structural information from simple optical spectroscopy techniques, with important implications in understanding the structure of nanoparticle films at liquid interfaces and their self-assembly.

Introduction

The ability to self-assemble nanoparticles (NPs) into macroscopic structures promises to revolutionize fields as diverse as diagnostics/sensing,[1-7] optics,[8, 9] and catalysis.[10, 11] The most common approach for such assemblies is to use a template to direct the formation of the structures. A liquid | liquid interface (LLI) is amongst the most convenient of such templates to direct 2D assemblies of NPs. The LLI itself forms spontaneously, is uniform, almost atomically defect-free, and self-healing.[12-16] It can capture NPs, driven by a reduction of its interfacial tension. These properties make the LLI in many ways preferable to even that of a solid interface in which defect-free surfaces require careful fabrication and even greater care is needed to avoid the introduction of defects at post-manufacturing phase. At the LLI, one may control the average distance between the NPs localized there through variation of electrolyte concentration in either or both phases. The presence of electrolyte screens the electrostatic interactions between the NPs. The higher the electrolyte concentration, the shorter the screening length and the closer to each other the NPs (settled at the interface) can get to form a dense array.

An obvious challenge in the characterisation of assemblies adsorbed at the LLI, as compared to solid interfaces, is the inability to employ direct imaging techniques, such as electron microscopies. To remedy the lack of such techniques, Turek *et al.*[17] demonstrated that plasmon coupling between the NPs could be used to assess the inter-particle separation with nanometre resolution. Despite this, it was clear that such experimentally derived inter-particle separations needed to be independently verified by alternative techniques.[17]

One of the few techniques capable of measuring *in situ* inter-particle separation is X-ray diffraction (XRD). X-ray wavelengths are of the order of 1 – 2 Å allow probing of structures on an atomic or molecular scale. When X-rays are incident onto an interface at or below the critical angle, such as in grazing incidence X-ray diffraction (GID), total external reflection will occur. The penetration depth of the X-rays are within the nanometre range, making GID very surface specific. Due to the very low angles used in GID (generally < 0.15°) the spot size of the X-ray beam is relatively large allowing sampling over a large area of the surface. Therefore, GID can provide information on the lateral and vertical arrangement of NP arrays over macroscopic areas. Consequently X-ray scattering presents a valuable tool for investigating surfaces, thin films and in particular liquid | liquid or liquid | air interfaces.[18, 19] X-ray reflectivity and GID has previously been used to examine the assembly of small GNPs (1 – 6 nm in diameter) at the liquid | air[20-23] and liquid | liquid interface.[24-26] These studies followed the structural arrangement of NPs during the

[a]*Department of Chemistry, Chemical Physics Section, Imperial College London, Exhibition Road, South Kensington, London, SW7 2AZ, United Kingdom.*
[b]*Department of Chemistry, University of Bath, Claverton Down, Bath, BA2 7AY, United Kingdom.*
Electronic Supplementary Information (ESI) available: [details of any supplementary information available should be included here]. See DOI: 10.1039/x0xx00000x

formation or compression of the NP layer and provided quantitative information on the in-plane and out-of-plane structure of the assembled NPs.[20-24, 26] Therefore the precision of X-ray reflectivity and diffraction in elucidating the interfacial properties makes it a perfect technique for referencing the plasmon ruler.[17]

In the work by Bera *et al*.[25] voltage-tunable counterion-mediated interactions between the NPs were used to control the lattice spacing of the 2D array. Herein, we utilize X-ray methods to study the assembly of 12.8 nm diameter gold NPs (functionalized with 12-mercaptododecanoic acid (MDDA)) at a water | 1,2-dichloroethane (DCE) interface (Figure 1 (a)). In this case the structure of the layer is tuned by systematic variation of the ionic strength in both the aqueous and organic phases. We go one step further from the plasmon ruler study[17] and investigate the assembly of NPs when an electrolyte is used in the organic phase, presenting the first report of NP assembly at the LLI using only organic phase electrolyte. The addition of electrolyte in either phase enables us to control the in-plane inter-particle separations, characterized by X-ray reflectivity as well as grazing incidence X-ray diffraction. Furthermore, due to the larger size of the NPs it is also possible to use optical techniques to characterize the interface. Using the combination of these techniques, we demonstrate that it is possible to calibrate the plasmon ruler at the LLI; allowing optical reflectance to accurately quantify inter-particle separations in a fast and simple manner.

Results and Discussion

Gold NPs were fabricated by the Tukevich-Frens method[27, 28] to produce NPs of diameter 12.8 ± 0.9 nm as determined from transmission electron microscopy, TEM (Figure 1 (b)) with a bulk localized surface plasmon resonance (LSPR) of 525 nm after modification with MDDA (Figure 1 (c)). A narrow NP size distribution is important for the X-ray reflectivity and diffraction experiments as it will allow the accurate calculation of structural details. The NPs are functionalized with a charged ligand (MDDA) to provide electrostatic repulsion between the NPs which can be screened with an electrolyte. The average interparticle separation between the NPs at the LLI is varied by tailoring their electrostatic interactions through the variation of electrolyte concentration in either aqueous (NaCl) or organic (TBA TPB) phase. The NPs assemble at the LLI interface by vigorously shaking the two phases together to form an emulsion. The emulsion reduces the distance the NPs in the aqueous phase need to diffuse to reach the interface. As the two phases separate out the NPs settle as a homogeneous layer at the LLI (Figure 1 (a)).

The NP films are analysed by both optical reflectance and X-ray reflectivity and diffraction (Figure 1 (a)). Details of NP surface coverage and spacing at the LLI is extracted from X-ray reflectivity and GID experiments. Changes in the plasmon resonance of the NPs as they come closer together and their plasmons begin to couple is observed by optical reflectance measurements. The optical characteristics are then systematically compared with X-ray data. A quantitative

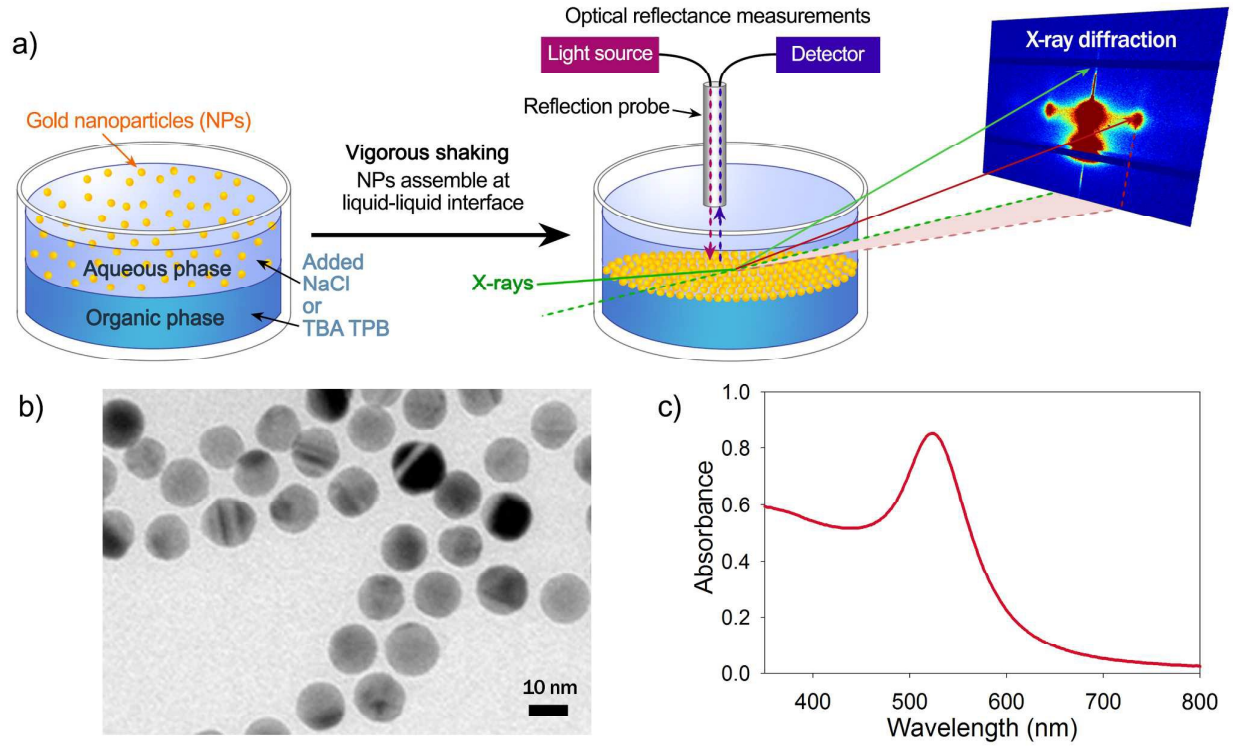

Figure 1. a) Schematic describing the self-assembly of gold NPs at the water – DCE interface when either NaCl or TBA TPB is added to the aqueous or organic phase. The assembled NP layer is analysed by X-ray reflectivity and diffraction to obtain structural information and is then analysed with optical reflectance to gain information on the plasmon coupling between the NPs. b) TEM image of prepared gold NPs. c) Absorbance spectra of the MDDA modified gold NPs.

structural dissection of the NP layers by X-ray reflectivity and diffraction combined with the optical plasmonic properties of the NP layers will not only benefit as a plasmon ruler but will also contribute new insights into the self-assembly behaviour of NPs at liquid interfaces.

X-ray specular reflectivity (XRR) from interfaces can be used to determine the change in electron density normal to the interface, with all in-plane detail effectively averaged. A typical XRR pattern shows total reflection of X-rays below a critical angle, which is normally defined by the magnitude of the change in electron density between supernatant and solution layer. The reflectivity then declines rapidly as a function of scattering vector Q, defined by the incident angle, θ and wavelength, λ;

$$Q = \frac{4\pi \cdot \sin(\theta)}{\lambda}. \quad (1)$$

In the NP system studied here, the very high electron density of the NPs leads to a virtual critical angle, which is very sensitive to the density of NP at the interface. In addition, the NP layer structure adds a Fourier component to the XRR profile, which is sensitive to the layer thickness, density and roughness. By subsequently fitting the reflectivity profile to a model profile, it becomes possible to extract the interfacial parameters which give rise to the observed profiles — principally the surface coverage, NP radius and displacement from mean interfacial position.

Figure 2 (a) shows the effect of adding NaCl to the aqueous phase on the assembly of the NP layer and their representative X-ray reflectivity profiles. For the higher NaCl concentrations, total reflection of X-rays is seen to extend to almost ten times the critical Q value for the interface alone. The low Q region is extremely sensitive to the average density of gold at the surface, and therefore the surface coverage of the NPs. The position of the fringes around 0.1 Å^{-1} are a sensitive measure of film thickness, and so with a model of the NPs, one can extract these two parameters independently.

The reflectivity curves were fitted using the RasCal[29] implementation of the Abeles layer method,[30] with a custom layer model simulating the NPs at the interface (Figure 2 (a)). Rather than fitting individual thicknesses, and layer densities, an approximation to the interface structure is built using a simple set of parameters. The NPs are assumed to have a spherical structure, consisting of a gold core with density of the bulk value of the metal with a low density MDDA capping layer of 1.5 nm thickness. The interface is sliced into 100 layers of equal thickness parallel to the surface normal defined by the variable fitted radius of the NP. Each theoretical layer contains spherical segments of the NPs, with their volume fraction defined by their position from the centre[31] and the layer thickness, and the overall surface coverage.

The volume of each spherical frustrum is given by

$$V = \frac{1}{6}\pi h \cdot (3a^2 + 3b^2 + h^2), \quad (2)$$

where a and b are the radii of the larger and smaller circles

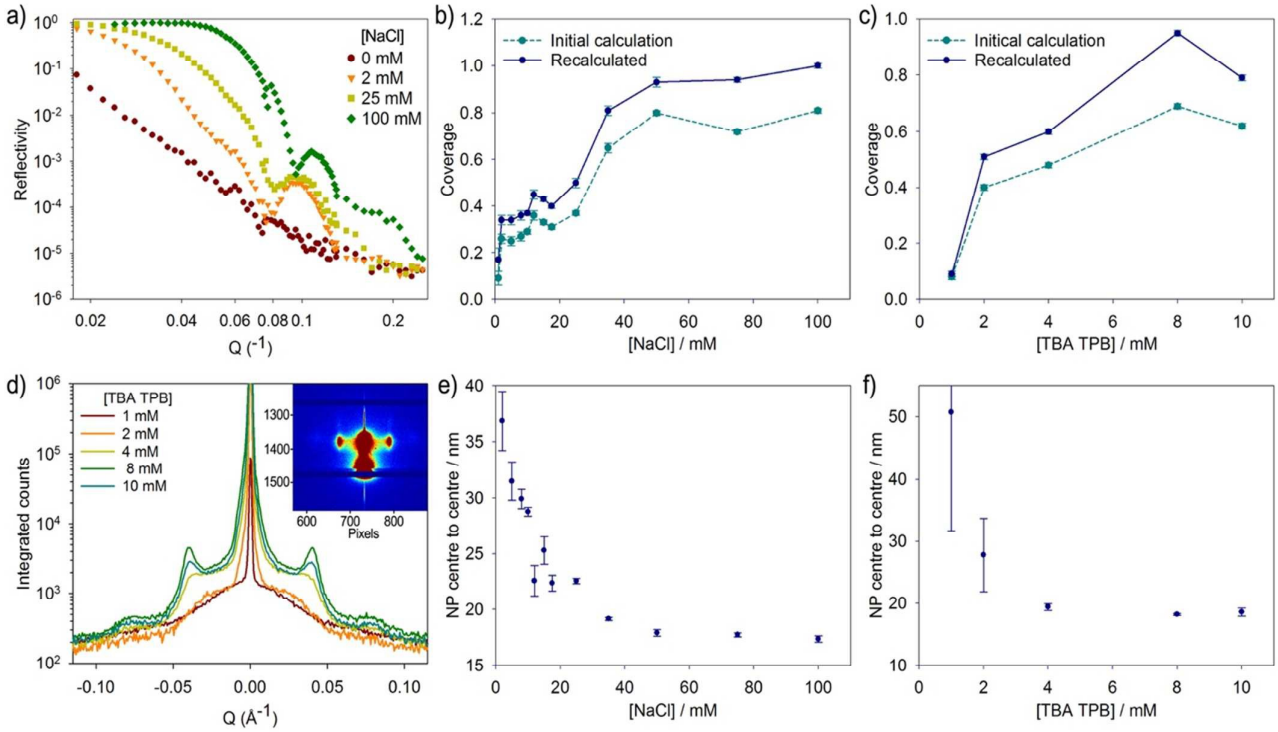

Figure 2. a) Reflectivity profiles for NP layers prepared at a few select NaCl concentrations. Coverage of NPs at the liquid | liquid interface assembled at various concentration of NaCl in the aqueous phase (b) and TBA TPB in the organic phase (c), showing both initial calculations and recalculations after taking into account NP interspacing from GID measurements. d) Profile of the horizontal cut along Q_X ($Q_Z = 0.06$ Å^{-1}) from the GID pattern of the NP array prepared at various TBA TPB concentrations with the GID pattern for 8 mM TBA TPB shown in the inset. NP centre to centre spacing for NP layers prepared at varying NaCl (e) and TBA TPB (f) concentrations.

cut across the sphere, and h is their separation. The residual volume of the calculated layer is then filled up by a linear combination according to height, relative to the interface, of the sub- and superphases. The scattering length density of each layer can then be calculated using the values for pure gold, water and DCE. Note the effect of using a more conventional sigmoidal LLI model, and allowing the position of the NPs to move relative to it, did not increase the quality of the fits, and made computation slower. The coverage was fitted by assuming a 2-D hexagonal close packing parameter of 0.9086, and adding for the presence of the capping component fatty layer (MDDA, thickness 1.5 nm). The position of individual NPs at the interface was allowed to vary from the mean by a Gaussian distribution, adding to the experimental resolution. Data were fitted using a simplex algorithm until the χ^2 factor reached a minimum — typically around $\chi^2 = 1$.

Data at higher NaCl concentrations can be fitted successfully using this simple model, but there is a subtlety in the scattering patterns for a few samples at lower concentrations, as seen in the fits for 2 mM NaCl in SI Figure 1. The fits for a single layer of NPs simply misses the feature around 0.05 $Å^{-1}$, which can only be fitted if two layers of NP are invoked at the interface, with a centre of mass displacement of the second layer close to the radius of the NPs, and a significant fraction (in this case 40 %) in the second layer. However, there was no evidence of any second layer of NPs in the TBA TPB reflectivity profiles, even at the lower coverages. Typically X-ray scattering studies of NPs at liquid | liquid or liquid | air interfaces show multilayer formation when the NP density at the interface is high such as when a packed monolayer of NPs is laterally compressed to induce buckling in the film, forming bi- or tri-layers of NPs.[20-24] One explanation for bilayers observed at low NaCl concentrations could arise from the assembly method – due to particles assembling to the interface once the two liquids are emulsified, the total interfacial area is massively increased. This leads to an 'excess' of NPs adsorbing to the emulsion LLI that the equilibrium interfacial area cannot accommodate. Due to the strongly repulsive forces between the particles instead of the usual buckling that such interfaces undergo, the excess particles are in fact desorbed from the interface in this system. This is supported by the fact that upon equilibration it is possible to see particles desorbing by eye (an optical density gradient arises close to the interface when the emulsion's droplets merge). It follows then that the desorbing particles have to explore the potential energy landscape around the interface and perhaps a local minimum exists away from the equilibrium position of the particles. The reasoning as to why such a minimum may exist at all could be due to the fact that despite the particles' geometry being that approaching a sphere, the vast majority of particles are in fact highly facetted – this may in turn mean that even if the particle is just touching the interface, it is still providing a relatively strong stabilization to the interfacial tension (*cf.* a perfect sphere for which the area of contact with the interface if just touching it would be negligible). Given this logic, the observation of these bilayers only at low NaCl concentrations may therefore be a result of the fact that not as many particles are desorbed as the NaCl concentration is increased (because the interface can accommodate more particles due to the reduced screening length, the particles adsorbed in the emulsion becomes comparable to that which the equilibrium interface can accommodate).

Another interesting result of the bilayer model is demonstrated in SI Figure 3. If the peak originating from one of the particles is fitted and subtracted from the scattering length density of the bilayer model, then a sudden drop or increase is seen in the density. This is a result of the fact the between the 2 limiting cases is the density difference of the interface itself. It is unfortunately not possible to precisely pinpoint the position of this interface, however from the bilayer model it becomes possible to narrow down the range of values where it can exist. Interestingly, this suggests that a range of values of the three phase contact angle can be elucidated. Determination of these critical values warrant further investigation using such procedures as freeze-fracture shadow-casting cryo-scanning electron microscopy.[32] Another interesting observation is that if the bilayer model is accurate and the range of values of the interfacial position to be believed, then the majority of the particles are more submerged in the organic phase (in the case of SI Figure 3 (a) the centre of the particle is just below the interfacial line, while for SI Figure 3 (b) most of the particles are fully submerged in the DCE and only just touch the interface).

At low electrolyte concentration screening of electrostatic interactions is weak which results in low interface coverage by NPs. Therefore, observation of bilayers at electrolyte concentration as low as 2 mM NaCl is a bit counterintuitive. But at the same time, there are examples of self-assembling of multilayers at low NP coverage of the interface. For instance, Sanyal *et al.* reported formation of 8 nm wide clusters of NPs, 3 layers thick, with large cluster-cluster spacing of 18 nm.[26, 33] However, their study examined the synthesis of 1.2 nm diameter NPs during a reaction at the water – toluene interface, and so the structure of the film is most likely attributed to the kinetics of NP formation. Indeed, in that work the X-ray diffraction data changes as the reaction proceeds due to the constant repositioning of NPs. The physical reasoning for the existence of such bilayers in our case is not yet well understood and will require further investigation.

Table 1 Parameters obtained from **GID** patterns for NP layers assembled at the water – DCE interface with **NaCl in the aqueous phase.**

[NaCl]/mM	Peak position/Å^{-1}	d-spacing/nm	NP centre to centre /nm	Peak Height /counts	Gaussian peak widths σ /Å^{-1}
2	0.0197	31.9 ± 2.3	36.8 ± 2.6	399.2	3.1 x 10^{-3}
5	0.0230	27.3 ± 1.5	31.5 ± 1.7	310	1.2 x 10^{-3}
8	0.0242	25.9 ± 0.7	29.9 ± 0.9	749	3.9 x 10^{-3}
10	0.0252	24.9 ± 0.3	28.8 ± 0.4	1369	2.8 x 10^{-3}
12	0.0321	19.5 ± 1.2	22.6 ± 1.4	1014	4.7 x 10^{-3}
15	0.0287	21.9 ± 1.1	25.3 ± 1.2	213	3.6 x 10^{-3}
17.5	0.0324	19.4 ± 0.6	22.4 ± 0.7	579	4.3 x 10^{-3}
25	0.0322	19.5 ± 0.2	22.6 ± 0.2	1425	3.4 x 10^{-3}
35	0.0378	16.6 ± 0.1	19.2 ± 0.1	1707	3.6 x 10^{-3}
50	0.0405	15.5 ± 0.3	17.9 ± 0.3	637	3.2 x 10^{-3}
75	0.0408	15.4 ± 0.2	17.7 ± 0.2	1252	3.2 x 10^{-3}
100	0.0418	15.0 ± 0.3	17.4 ± 0.3	884	2.7 x 10^{-3}

Table 2 Parameters obtained from **GID** patterns for NP layers assembled at the water – DCE interface with **TBA TPB in the organic phase.**

[TBATPB]/mM	Peak position/Å^{-1}	d-spacing/nm	NP centre to centre /nm	Peak Height /counts	Gaussian peak widths σ /Å^{-1}
1	0.0143	44.0 ± 15.0	50.70 ± 19.0		
2	0.0261	24.1 ± 5.1	27.80 ± 5.9	63	2.3 x 10^{-3}
4	0.0373	16.8 ± 0.5	19.4 ± 0.5	838	4.9 x 10^{-3}
8	0.0398	15.8 ± 0.1	18.2 ± 0.2	2973	3.1 x 10^{-3}
10	0.0390	16.1 ± 0.6	18.6 ± 0.7	1738	4.5 x 10^{-3}

After fitting the reflectivity profiles, the NP surface coverage at the interface and other structural parameters could be determined (summarised in SI Table 1 & 2). The NP surface coverage for varying NaCl and TBA TPB concentrations is plotted in Figure 2 (b) & (c) respectively. With increase of electrolyte concentration in the aqueous phase, the surface coverage increases significantly in the domain of low concentrations (0 – 35 mM NaCl) followed by a slower increase over the range 35 – 100 mM. For TBA TPB electrolyte in the organic phase, the interface coverage by NPs increases steadily until the concentration reaches 6 mM, after which the coverage plateaus.

The initial calculation of the fitted coverage in the reflectivity measurements relied on the assumption that the NPs are hexagonal packed in monolayer, with the minimal inter-particle separation equal to the fitted diameter of the NPs (the intrinsic diameter of gold NP plus 1.5 nm MDDA layer). With the extra separation implied by the limiting GID *d*-spacing (Table 1 & 2), this can be corrected and leads to higher calculated surface coverages. A discussion of the correction for surface coverage values after taking into account the limiting GID d-spacing is included in the supporting information. The corrected coverages are shown in SI Table 1 & 2 and plotted alongside initial surface coverage values in Figure 2 (b) and 2 (c) for varying NaCl and TBA TPB concentrations respectively.

Each of the samples used in the reflectivity measurements were measured with GID to investigate the in-plane correlations from which NP centre to centre spacing can be calculated. Incident angles were chosen to be close to the critical angle for the LLI, $Q_z = 0.06$ Å^{-1}, to give the greatest sensitivity to the surface, balanced with the need to sustain a good footprint on the sample. Figure 2 (d) inset shows a typical diffraction pattern which was obtained from the 8 mM TBA TPB sample. The important features are the central line at ~730 pixels in the x-direction, and the two Bragg peaks at $x =$ ~670 and ~790 at y -pixels corresponding to the specular reflection. These can be seen to show weak Bragg rods at higher (y -direction) angles, demonstrating the 2-D surface nature of the film, and very weak 2nd order diffraction peaks at lower and higher x -values.

The data are more easily visualised by integrating the y -axis values from pixels 1340 – 1410, and plotting as a function of Q_x . Figure 2 (d) shows the same data presented in this way. The second order peaks can now clearly be seen. The first order in-plane diffraction peaks were then fitted with a sloping background and Gaussian curve to yield peak positions, which were converted to d -spacing. With the assumption of hcp packing, the NP centre-to-centre distances as well as peak heights and Gaussian peak widths, σ , were extracted. Table 1 & 2 show the data for the effects of NaCl and of TBA TPB concentrations on the in-plane structure. Although there was some broadening in the central $Q = 0$ Å^{-1} peak for the 1 mM NaCl sample, it was not possible to resolve any in-plane peaks and therefore the data is not presented. Additionally the peak position for the 1 mM TBA TPB sample is close to the central peak, and so the position is estimated from the raw data, rather than fitted, hence the large error in centre-to-centre spacing observed. The error in determining the interparticle

spacing increases with lower electrolyte concentration (fewer NPs at the interface) as the Bragg peaks sit close to the central $Q_x = 0$ Å^{-1} peak, thus making them harder to resolve.

Figure 2 (e) shows a plot of NP centre-to-centre distance as a function of aqueous phase concentration of NaCl. We are able to tune the centre to centre NP spacing down to 17.35 nm corresponding to a surface-to-surface gap of 4.5 nm (taking into account the diameter of the NPs are 12.8 nm). In principle, NPs are not expected to come closer together than 3 nm, because of the steric repulsion among NPs coated by ~ 1.5 nm thick layer of adsorbed MDDA, but they in fact stop to approach each other earlier, presumably due to unscreened Coulombic repulsion at such short distances. NP separation drastically decreases with increasing NaCl concentration until 50 mM NaCl after which the inter-particle distance remains relatively constant (Figure 2 (e)).

For added TBA TPB in the organic phase the centre to centre NP distances can be reduced to 18.2 nm or a surface to surface gap of 5.7 nm (Figure 2 (f)). We obtained the centre-to-centre spacing only for four samples (not including the 1 mM TBA TPB sample which was estimated from raw data), among which the trend cannot be clearly resolved. But it can be inferred that the major changes in interparticle spacing occur below 4 mM TBA TPB and therefore, and it would be interesting to perform in the future GID experiments in this concentration range. The interparticle spacing is consistent with the trend observed for TBA TPB surface coverage, particularly the onset of a plateau above 4 mM TBA TPB.

One of the striking results is that the width of the diffraction peaks, measured by the fitted σ values of the Gaussians is remarkably similar at all concentrations of NaCl and TBA TPB. The width of the in-plane diffraction peaks is a convolution of resolution and effects due to domain size. This implies that the average size of the domains is not changing with electrolyte concentration. It is possible to make a rough estimate of the domain size using the Scherrer equation[34]

$$\tau = \frac{K\lambda}{\beta \cdot \cos(\theta)}, \qquad (3)$$

where τ is the mean size of the ordered domains, K is a shape factor typically ≈ 0.9 and β is the Gaussian's full width at half-maximum (FWHM). At the low angles used here, $\cos(\theta) \approx 1$ for all cases, so for an average σ value of 3.48 x 10^{-3} Å^{-1} this yields an average Scherrer domain dimension of 142 nm. The Scherrer domain size is usually taken as the square root of the crystallite area, so for close-packed NPs, this suggests around 200 nanoparticles per coherent diffracting unit as the minimum size. It should be noted that the applicability limit of the Scherrer equation is about 100 nm.[35]

Although there is unequivocal evidence from the reflectivity data that at lower NaCl concentrations bilayers form, at higher NaCl and all TBA TPB concentrations the reflectivity shows that only single layers formed at the LLI (SI Table 1 & 2). GID data suggest the two dimensional nature of the films as demonstrated in the weak Bragg rods seen in Figure 2 (d) in the 8 mM TBA TPB sample, and these are also seen in all concentrations above 35 mM NaCl. Due to the lower intensity of in-plane scattering at concentrations less than 35 mM, none of the weak Bragg rods are visible, but there is no qualitative change in the extended shape of the measured peaks. Going from a truly two-dimensional layer at high concentrations to a corrugated quasi 2-D layer at lower values does not seem to alter the general shape and results from the diffraction measurements.

Optical reflectance can be used to probe the changes in the plasmonic response of the NPs as they come closer together and their localized plasmonic modes couple. The expected trends in the reflection spectra with the increase of electrolyte concentration in either phase are the red-shift in the reflectance maxima (λ_{max}), overall increase in the reflectance (R_{max}), and peak broadening as the NPs come closer to each other.

A previous plasmonic ruler work[17] from our group has demonstrated the assembly of NPs at the interface of a droplet of water suspended in DCE, by utilizing transmission spectroscopy. This provided information on the effect of changes in the localized surface plasmon resonance (LSPR) due to plasmon coupling among the NPs. In our present work we employ a specular reflection technique configured at normal incidence; as such measurements give information on light scattered back, they do not directly quantify absorbance of light and hence, the reflectance peak may be positioned slightly away from the wavelength of LSPR transmission measurements that are affected by both absorbance and scattering. At the same time, shifts in the reflectance maxima (λ_{max}) still correlate with changes in the LSPR of the constituent NPs. In fact, Kedem *et al.*[36] demonstrated reflectance spectroscopy to be more sensitive to changes in NP LSPR than transmission spectroscopy which is dominated by absorption. For reference, in SI Figure 4 we have plotted the relationship between LSPR position (from transmission spectroscopy) and the maximum position (λ_{max}) of the reflectance spectra. It can be seen that the optical reflectance measurements are more sensitive to changes in NP LSPR as λ_{max} red-shifts by a greater amount relative to the transmission measurements.

The reflection spectra of the NP layer as a function of increasing concentration of NaCl in the aqueous phase and TBA TPB in the organic phase (Figure 3 (a) and (b) respectively) demonstrate the expected general trends: the increase of the population of NPs at the LLI causes a red-shift of the peak, increase in overall reflectance, and spectral broadening. These trends are further displayed in Figure 3 (c) and (d), with λ_{max} being tuneable between 540 nm and 610 nm and R_{max} varying between 1 and 13 %, as a function of NaCl or TBA TPB concentration.

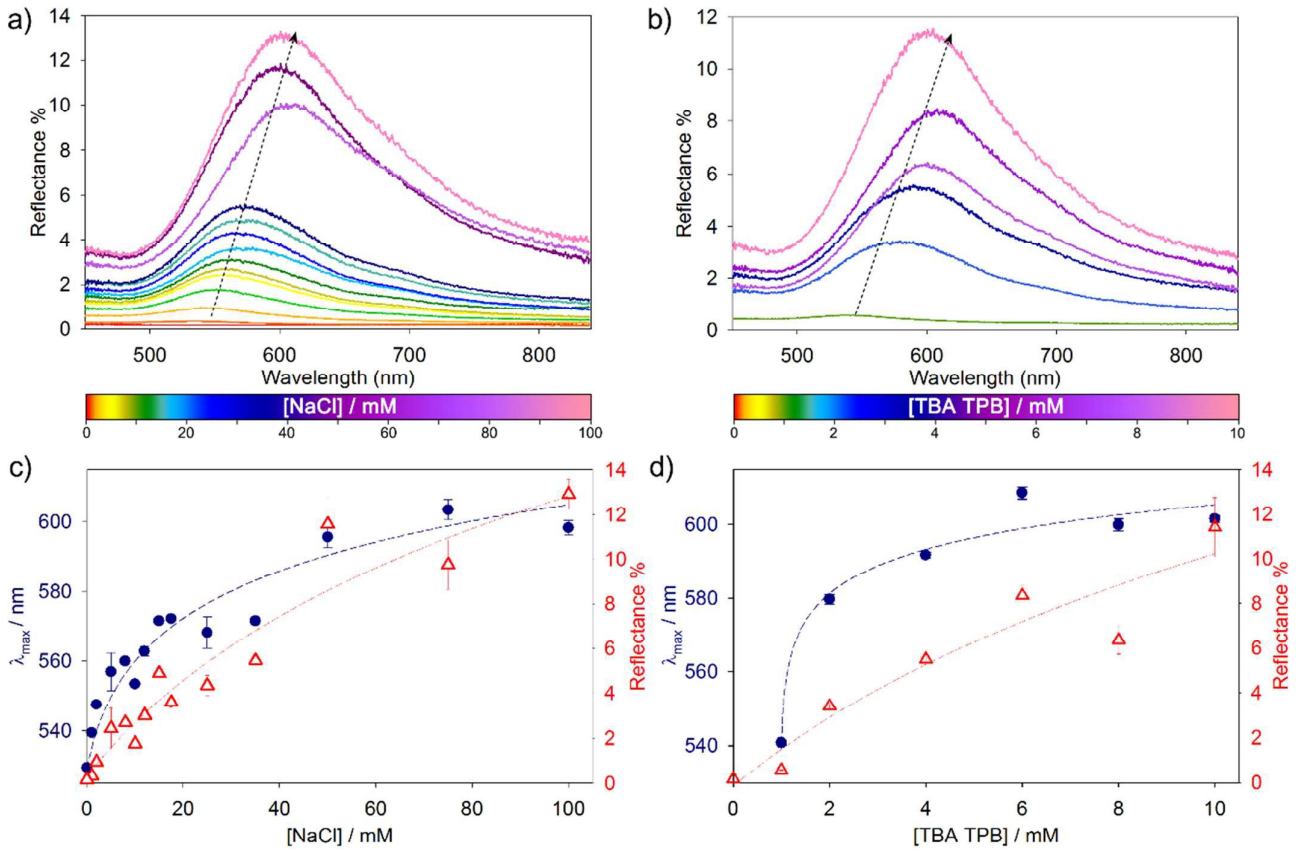

Figure 3. Reflectance spectra for NPs assembled at the water-DCE interface at varied electrolyte concentration, (a) NaCl in the aqueous phase, and (b) TBA TPB in the organic phase. Wavelength maxima positions (Δ) and reflectance at maximum (●) of the NP films extracted from reflectance plots for varying NaCl (c) and TBA TPB (d). Note: reflectance spectra shown are the average of five reflectance spectra taken from different areas on each sample.

It should be noted that without any electrolyte in either phase no NPs or very few are assembled at the interface, and not detectable by the reflectance measurement. On the other hand we cannot increase the electrolyte concentration beyond the certain limit, here 100 mM NaCl, as above it NPs tend to agglomerate in the bulk and at the LLI, causing disorder in their arrangement and leading to a dramatic reduction in the reflectance.

As in the previous plasmonic ruler study,[17] there is a red-shift in the spectra of layers assembled for up to 50 mM NaCl concentrations, followed by a plateau at higher ionic strengths. At the same time R_{max} continues to increase monotonously with NaCl concentration up to 100 mM NaCl. As λ_{max} is representative of the NP spacing, while R_{max} is indicative of surface coverage, these results imply that at higher electrolyte concentration the spacing between the NPs remains constant while the coverage of NPs at the interface continues to increase, which is contrary to X-ray reflectivity and GID results. However the reflectance technique implemented here is only semi-quantifiable in terms of R_{max}. The reflectance probe illuminates and detects from the same direction and so only sees a portion of the reflected light. As the coverage of the NPs at the interface increases more light is scattered back into the detector and variations in intensity will become more evident. (SI Figure 5 & SI Figure 7 (b)). Also variation of R_{max} can be explained through measuring only a dense closed-packed island. While best efforts were made to average reflectance data over five different areas, due to island formation R_{max} will be highly dependent on the probe location and so variations can occur. Therefore R_{max} measurements that collect only normally reflected light from a small specified area are, to a certain extent, limited. However R_{max} is still a good indicator for observing general trends in reflectance and can also distinguish when the NP layer has become disordered which will be evident from the film appearing matt and hence a drop in reflectance. The use of angle-varied reflectance or an integrating sphere in the future investigations could provide more quantitative information on the reflectance of the films.[37, 38] These techniques are harder to implement at buried

liquid interfaces but will additionally reveal important spectral features of the layer and so warrants future study.

A correlation of λ_{max} and R_{max} is presented in the supporting information. SI Figure 5 shows that at reflectance higher than 4 % and maxima positions higher than 564 nm there is a significant spread between λ_{max} and R_{max} values. For example, for three samples yielding identical λ_{max} at 604 nm the reflectance differs from 8 to 12. A lower R_{max} yet at longer wavelength position could be explained by disorder and aggregation in a close packed layer. At such high ionic strengths the charge on the NPs are screened to such an extent that the Coulomb repulsion between NPs is no longer strong enough to prevent aggregation. An aggregation of NPs will cause a red-shift, whereas any breakdown of ordering in the NP layer will cause a decrease in reflectance along with broadening of the whole reflection spectrum. Hence, there is a need to take into account the entire shape of the reflectance spectrum, not only the peak height and position. However, a broadening of the curve does not necessarily go together with the red-shift of λ_{max} and decrease in R_{max}. For example, when the three data points displaying similar λ_{max} (~604 nm) but differing R_{max} (8, 9.5 and 12 % for 50, 75 and 100 mM NaCl, respectively) are normalised and plotted together (SI Figure 6), no broadening of the curve relative to each other is apparent. Therefore in this case the decrease in reflectance observed for the 50, 75 and 100 mM samples cannot be attributed to aggregation or disorder in the layer. Further, as interparticle surface-to-surface separations of less than 4.5 nm are not observed in the diffraction data, this would suggest that the NP layers formed in this study are not aggregated. A similar position of the maximum with yet differing reflectance is most likely inherent to the limitations of the specular reflectance technique used in this study and its inability to provide true quantitative R_{max} values as discussed earlier. The results are fairly reproducible, but there is some minor degree of variation among samples prepared at a given electrolyte concentration. Repetitions of samples prepared at certain NaCl concentrations were performed to determine the precision of both the position and magnitude of the reflectance (SI Figure 7).

For TBA TPB R_{max} is seen to increase steadily over the TBA TPB concentration range. λ_{max} red-shifts significantly after only 2 mM TBA TPB then plateaus from ~ 6 mM TBA TPB onwards. R_{max} for the 8 mM TBA TPB sample appears lower than expected values from the apparent trend. A decrease in R_{max} may be due to lower surface coverage but as the XRR

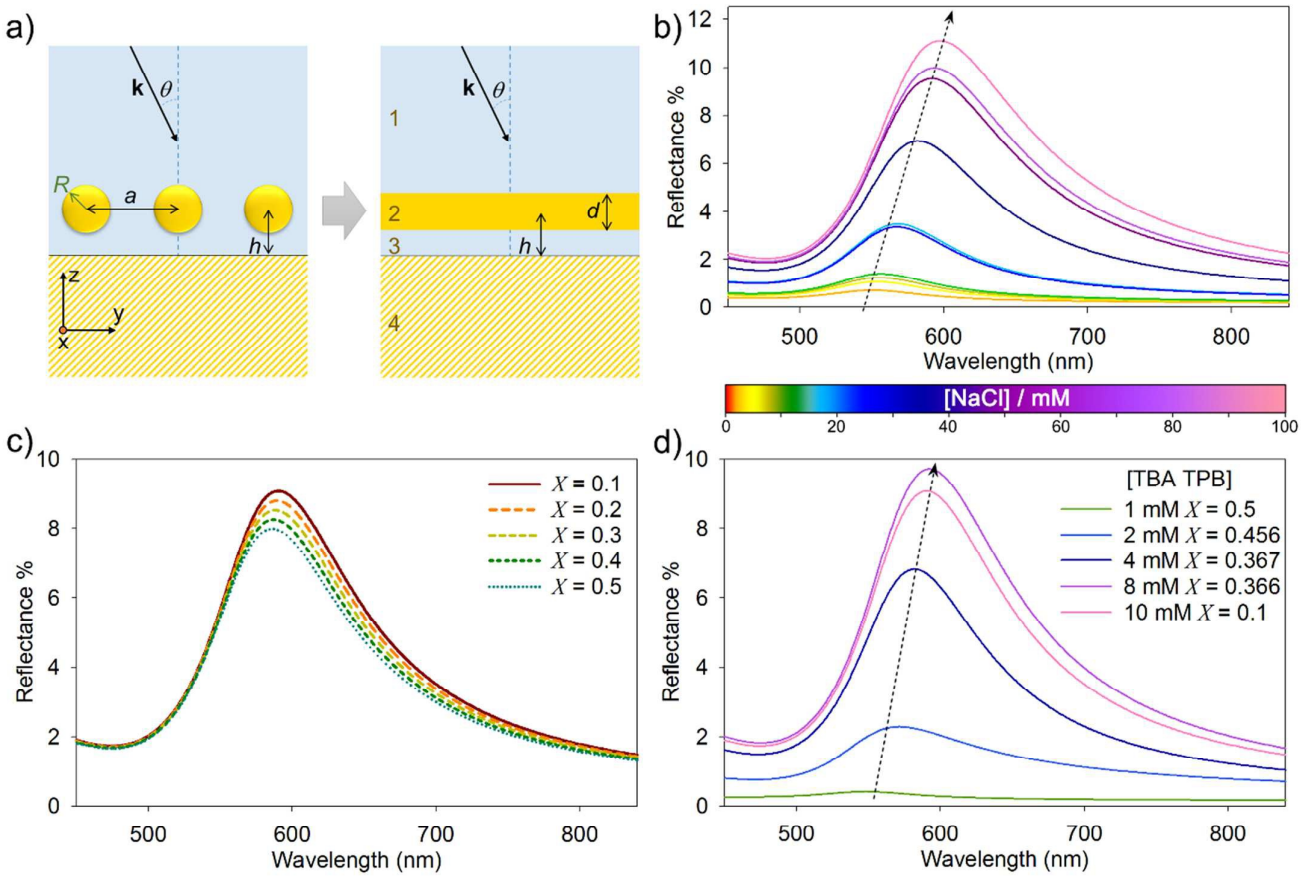

Figure 4. Theoretical analyses of the reflectance spectra. a) Schematic of the '4 layer stack model' of the 'effective medium theory'. b) Reflectance spectra calculated for experimentally determined distances between the NPs for the specified concentration of NaCl in water. c) The effect of the relative position of the NPs with respect to the LLI on the calculated reflectance spectra, shown for a fixed value of a, corresponding to TBA TPB concentration of 10 mM (cf. Table 2). d) Reflectance spectra calculated for experimentally determined distances between the NPs, which also incorporate the estimated position of NPs along the interface through fitted parameter X, for the specified concentrations of TBA TPB in the organic phase.

experiments show the 8 mM TBA TPB sample as the highest coverage of the set, this is likely not the case. Therefore this decrease in reflectance can be due to either experimental error due to focussing discrepancies or the limitations in quantification from the specular reflection technique, or/and it is not excluded that agglomeration of NPs at the LLI may eventually start already from 8 mM concentrations.

To rationalize the reflectance spectra from a LLI populated with NPs, we extend and apply the existing effective medium theory.[39, 40] The expressions for effective polarizabilities in Refs[39, 40] have been simplified to ignore the effects from image contributions as the difference between refraction indices of water and DCE phases is negligible. Rather, a new parameter is introduced to capture the relative position of NPs piercing the interface. We also extended the reflectance calculations to include the effects arising from experimentally-reported distribution in NP size and lattice spacing. This is implemented by weighted averaging of optical reflectance spectra, using dispersion parameters in calculation. Incorporation of both two effects broadens the spectra and bring them close to the experimentally observed ones. This theory is formally valid in the long wavelength approximations: $ka \ll 1$ (consequently, $kR \ll ka/2 \ll 1$) where k is the wave vector of the incident light. The latter allows us to model the plasmonic response of NPs in dipolar approximation. For the NP arrays studied in the above described experiments, this approximation should be perfectly applicable. We first model the optical characteristics of the NP layer assuming an ordered system of NPs (here, gold nanospheres of radius R) occupying all sites of a two-dimensional (2D) hexagonal lattice with a lattice constant *a*. The effective polarizability of an individual NP interacting with all other NPs in the 2D array along the directions parallel ($\|$) and perpendicular ($\perp$) to the LLI can be expressed as:[39]

$$\beta_{\|}(\omega) = \frac{\alpha(\omega)}{1 + \alpha(\omega)\frac{1}{\varepsilon_2}\left(\frac{-1}{2}\frac{U_A}{a^3}\right)}, \quad (4a)$$

and

$$\beta_{\perp}(\omega) = \frac{\alpha(\omega)}{1 + \alpha(\omega)\frac{1}{\varepsilon_2}\left(\frac{U_A}{a^3}\right)} \quad (4b)$$

In the above equations, $U_A = \sum_i {}' \sum_j {}' \frac{1}{\left(i^2 + j^2 - ij\right)^{3/2}} = 11.031$ is the Topping lattice sum over all NP coordinates on a hexagonal lattice; $\alpha(\omega)$ denotes the frequency-dependent isotropic polarizability of each free-standing sub-wavelength nanosphere, embedded in a liquid with dielectric constant ε_2 and is given by

$$\alpha(\omega) = \varepsilon_2 R^3 \frac{\varepsilon_{\mathrm{NP}}(\omega) - \varepsilon_2}{\varepsilon_{\mathrm{NP}}(\omega) + 2\varepsilon_2}, \quad (5)$$

where $\varepsilon_{\mathrm{NP}}(\omega)$ is the permittivity of the NP material (here, gold). The latter can be approximated by the Drude–Lorentz model, with the formulae and the values of parameters that fit experimental data[41] provided in the SI. For the NPs with diameter of around 12.8 nm, we have additionally incorporated the size-dependent corrections to the permittivity model to account for enhanced scattering losses of surface electrons at NP boundaries.[42, 43] In what follows, the 2D layer of NPs can be further characterized by an anisotropic dielectric tensor, whose parallel $\varepsilon_1^{\|}(\omega)$ and perpendicular $\varepsilon_1^{\perp}(\omega)$ components satisfy the following relations:[39, 40]

$$\varepsilon_1^{\|}(\omega) = \varepsilon_2 + \frac{4\pi}{a^2 d}\beta_{\|}(\omega), \quad (6a)$$

and

$$\frac{1}{\varepsilon_1^{\perp}(\omega)} = \frac{1}{\varepsilon_2} - \frac{1}{\varepsilon_2^2}\frac{4\pi}{a^2 d}\beta_{\perp}(\omega) \quad (6b)$$

where d is the characteristic thickness of the NP layer.[44]

Thus estimated effective dielectric permittivity of the NP layer allowed us to adopt the '4 layer stack model' of the 'effective medium theory' developed in Ref.[40] in order to be able to calculate the reflectance spectrum from NP layer at the LLI (Figure 4 (a)). Our present study deals with water - DCE interface, and hence we adopted the following dielectric permittivity values — $\varepsilon_0 = 1.78$ for water and $\varepsilon_3 = 2.08$ for DCE. The reflection spectrum can then be calculated deploying the Fresnel scheme to estimate reflection coefficient $r^{(\mathrm{s,p})}$ for either s- or p-polarized excitation as mentioned in section 2.1 of Ref[40]. Note that, in the experiments only the case of normal incidence of light was considered, which allows us to set $\theta = 0$, implying that $r^s = r^p$. From these reflection coefficients the reflectance $R^{(\mathrm{s,p})}$ can then be easily calculated as $R^{(\mathrm{s,p})} = \left|r^{(s,p)}\right|^2$.

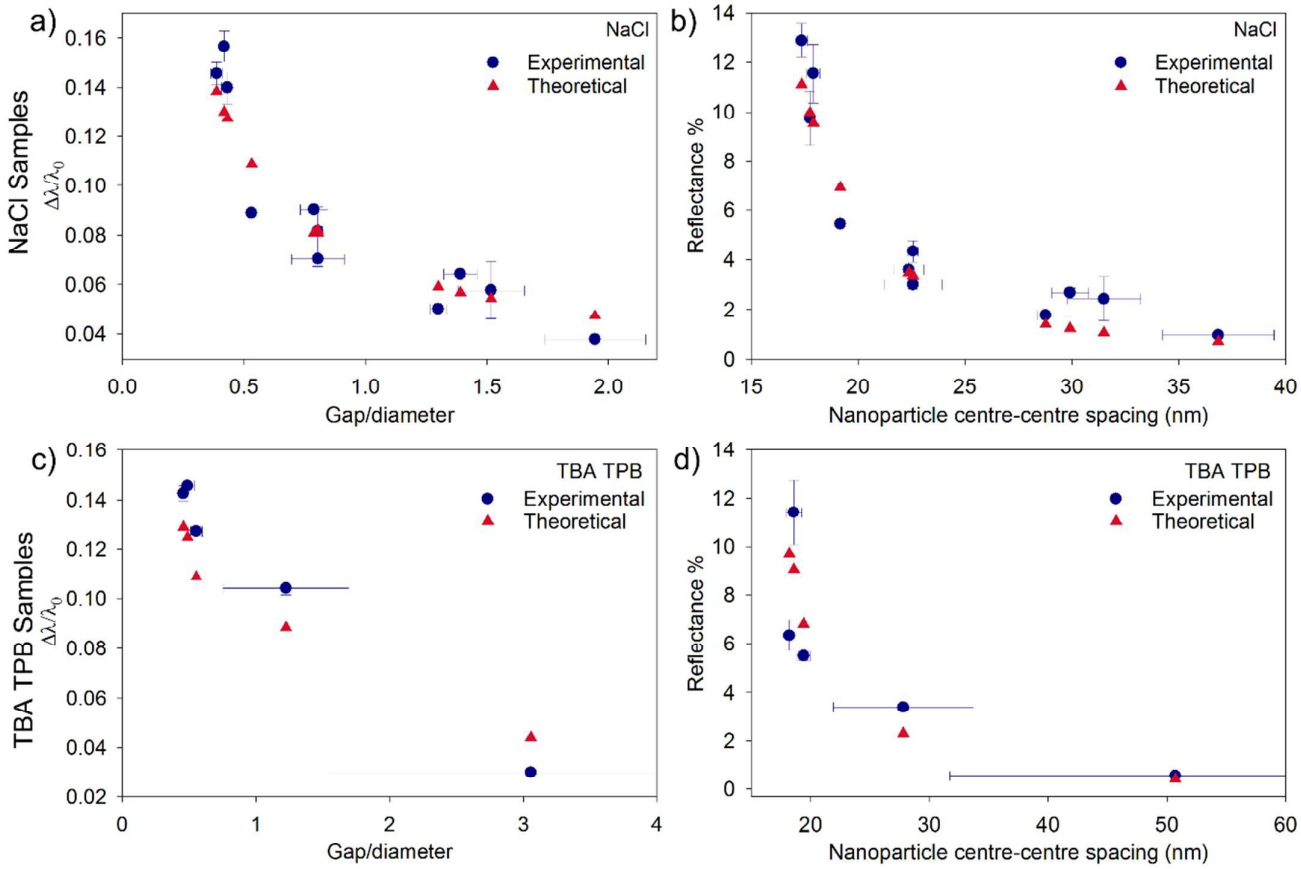

Figure 5. The wavelength fractional shift ( ) of the reflectance wavelength maximum of NP layers assembled at the water-DCE interface as a function of the ratio of the NP surface-surface separation to NP diameter for NaCl (a) and TBA TPB (b).) Reflectance for NP layers assembled with NaCl in the aqueous phase (c) and TBA TPB in the organic phase (d) as a function of NP centre to centre spacing. Experimental results (▲) are compared to theoretically derived data (●).

It is also important to note that as the NPs used in the experiment were polydisperse, we estimate the averaged reflectance from the NPs by assuming the NP radii values to follow a Gaussian distribution profile. From the experimental values we obtain estimates for the mean radius μ_R and standard deviation σ_R, which are discussed in details in the SI. To incorporate the spread in the inter-particle separation or the disorder found in lattice constant a (as measured experimentally) into the calculations, we further averaged reflectance by assuming parameter a to also follow a Gaussian distribution profile, where the mean and standard deviation parameters μ_a and σ_a used in calculations are listed in SI Table 3 & 4.

Instead of introducing the parameter σ_R (the position of the centre of NPs from an ideal interface) in the effective medium theory,[40] here we will put h , *i.e.*, we position the NPs exactly in the middle of the interfacial layer but vary the value of the background dielectric constant of the layer (ε_2) in which the NPs are embedded. This can be approximated by linear interpolation, $\varepsilon_2 = X\varepsilon_0 + (1-X)\varepsilon_3$, where X denotes the fraction of the NP volume immersed in water (*i.e.*, $X = 1$ means that NPs are located fully on the water side of the interface, whereas $X = 0$ means that they are completely embedded on the organic side).

In the case when NaCl electrolyte is added in the aqueous phase, we found that $X = 0.5$ (i.e., the NPs sitting half-way in water and half-way in DCE) could nicely match the experimental data. With these parameters we obtain the theoretical reflectance spectra as depicted in Figure 4 (b).

In the second case when TBA TPB electrolyte is added in the organic phase, theoretical calculations indicate that the NP layer gradually shifts towards the organic side with increase of the electrolyte concentration. This can be realized by observing the trend of the reflectance spectra calculated for lowering X , which could closely predict the experimentally measured reflectance at large electrolyte concentration (see Figure 3 (b) and Figure 4 (c)). So, for our calculations of theoretical reflectance spectra (as depicted in Figure 4 (d)) we

assumed the NP layer to be exactly at the interface (*i.e.*, $X = 0.5$) at low TBA TPB concentration of 1 mM. With increase in TBA TPB concentration when NPs slowly drift towards the organic side, we roughly approximated $X = 0.1$ at large TBA TPB concentration of 10 mM. Based on these simplifying assumptions, we further predicted the X values for intermediate concentration levels *via* linear interpolation. The above prediction of NPs drifting towards the organic side with increasing concentration of electrolyte in the organic phase, based on the best fit of our data, agrees well with the claims made by the Schlossman research group.[25]

Through combining the optical and diffraction results a plot of the wavelength shift and reflectance of the NP films as a function of the centre-to-centre NP spacing can be obtained (Figure 5). The plots are further combined with theoretical results which agree well with the experimental data. The data in Figure 5 (a) and (b) is presented as the wavelength shift scaled by the bulk LSPR ($\Delta\lambda/\lambda_0$) and NP gap scaled by the NP diameter as it allows the results to be applicable to any NP system[45] and serves as a calibration to the 'plasmon ruler'. However, as we present limited data for NPs assembled with TBA TPB in the organic phase we do not suggest its use as a plasmon ruler reference. For reference, λ_{max} as a function of centre to centre spacing is plotted for both NaCl and TBA TPB in SI Figure 8.

The wavelength shift for both NaCl (Figure 5 (a)) and TBA TPB (Figure 5 (c)) increases rapidly as the NPs come closer together. The strong red-shift in λ_{max} at small NP distances indicate strong plasmon coupling. The reflectance of the NP layers also increases rapidly as the NPs come closer together with the major changes in R_{max} observed when the NP centre to centre spacing is below ~25 nm for both NaCl (Figure 5 (b)) and TBA TPB (Figure 5 (d)).

A power-law dependence between the wavelength shift and the NP gap is observed for NP layers assembled with NaCl, similar to studies on the plasmon coupling between pairs of nanoparticles or nanoparticle-surfaces.[46-48] The wavelength shift decays rapidly at short NP interspacing until the gap between the NPs is approximately the same diameter as the NP. After which, the wavelength shift lessens indicating a decline in the near-field plasmon coupling between the NPs. The plasmon coupling between NPs plays a key role in applications such as surface enhanced Raman spectroscopy (SERS) and near-field optics. Huang et al. observed a universal power law dependence on both resonant wavelength shift and field enhancement with surface-surface gap regardless of geometry (particle–void, particle–particle, and particle–flat surfaces).[46] Consequently our plasmon ruler will be particularly useful in tuning plasmonic hotspots for Raman sensors where plasmonic enhancement is observed between 2 – 10 nm from the NP surface.[49, 50] This referencing tool will enable researchers to tune the NP spacing with a confident estimate of the NP separation through simple spectroscopic techniques without the need to perform involved synchrotron experiments. Due to the long chain thiol used in our study we observe a cap in the interparticle surface-to-surface spacing of 4.5 nm and so would not be ideal for exploiting or studying Raman enhancement. However, it would be interesting to observe the Raman response of such films as the nanoparticle spacing is decreased.

Conclusions

Application of three complementary experimental techniques — X-ray reflectivity, GID and optical reflectance — in combination with each other along with a simple yet adequate theory of optical response of such interfaces, enables unprecedented understanding of the structural properties of NP assemblies at the LLI. X-ray reflectivity and diffraction measurements revealed a decrease in NP interspacing and an increase in NP coverage at the LLI with increasing electrolyte concentration in either the aqueous or organic phase. Optical reflectance measurements correspondingly showed a red-shift in the reflectance maxima with increasing electrolyte concentration, attributed to an increase in plasmonic coupling between the NPs. Through combining the NP spacing as determined from GID experiments with the wavelength shift in the reflectance maxima we generated a plasmon ruler, which obeys a power law dependence of the wavelength shift on the NP gap. Thereby, it becomes possible to generate accurate structural information of the inter-particle separations at the LLI through optical spectroscopy in a fast and easy manner, with widely available equipment. It is hoped that the availability of such knowledge would promote further research into the exciting applications that plasmonic particles adsorbed at the LLI offer, as well as enable researchers to gain further fundamental understanding of the behaviour of such systems. Finally, these techniques have also suggested that a bilayer of non-aggregated particles may exist at the interface at low electrolyte concentration, an unexpected result given the low number of NPs adsorbed at the interface at those concentrations. The physical reasoning for the existence of such bilayers is not yet fully understood and will require further investigation. The preliminary TBA TPB results are interesting, especially as the assembly of NPs at the interface using electrolyte in the organic phase has not been done previously, and warrants a full study to further elucidate the underlying mechanism for formation layers of nanoparticles at the LLI.

The outlook of this study will have major ramifications in the fields of SERS, ordered plasmonic assemblies, and electrovariable NP arrays. It would be interesting to demonstrate control of the Raman response as NP surface coverage increases and inter-NP spacing decreases, working towards NP assemblies with fully tuneable homogeneous "hotspots". The system described herein is that of an ITIES (interface of two immiscible electrolytic solutions) in which the interface can be polarized in an electrochemical cell, and the

effect of the potential drop across the interface will affect/control the density of the interfacial array of NPs. As such, we did not exploit ITIES for voltage driven assembly in this study but such insights into the structure of NP assemblies described herein should support future research on electrovariable NP arrays. Additionally, further investigation should involve angular and polarization dependence of the reflectance from the NP films or, if experimentally possible, the implementation of an integrating sphere to fully reveal all important spectral features.

Materials and Methods

Gold nanoparticle fabrication

Gold NPs were synthesised by the Tukevich-Frens method[27, 28] the citrate (40 mg/100 mL) reduction of $HAuCl_4.xH_2O$ (17.24 mg of gold/100 mL) in water under reflux. The NPs were then functionalised with MDDA by reducing the temperature to 60 °C and adding 10 mg of MDDA dissolved in 0.5 mL methanol. The functionalization was allowed to take place over 5 minutes, before the heating was switched off and the mixture was allowed to cool to room temperature under stirring. The excess MDDA is not water soluble at room temperature, therefore the precipitated solid was removed through filtration with a 0.2 µm syringe filter. The resultant NPs yielded a diameter of 12.8 ± 0.9 nm (as assessed from TEM, Figure 1 (b)) and had a localized surface plasmon resonance (LSPR) maximum of 525 nm in the bulk (Figure 1 (c)). The as-made solution contained 5.0 x 10^{12} NPs per mL as calculated from UV-Vis absorption.[51]

Preparation of nanoparticle films at the liquid | liquid interface

We added 75 mL 1,2-dicholoroethane and 100 mL aqueous solution (containing 25 mL of the as-made NP solution, varying amounts of 1 M NaCl solution, topped up to 100 mL with ultra-pure water), to a wide-mouth soda lime-glass jar of 250 mL capacity (of 88 mm height and 73 mm diameter). Particle adsorption at the LLI was promoted through emulsification by shaking the bottle for 10 s. By vigorously shaking the containers small microdroplets were formed in which the average distance that the particles need to diffuse to adsorb to the interface gets reduced to the point where 10 – 15 s become sufficient to reach an equilibrium. The emulsion was then allowed to separate out into the 2 phases over a period of ≈ 5 minutes and any desorbed NPs were re-homogenized with the bulk aqueous phase by gentle agitation. A UV-Vis spectrum of the aqueous solution was recorded with a Nanodrop 2000c spectrometer following the emulsification of each sample in order to correct for absorbance losses in the subsequent optical reflectance measurements.

Optical Reflectance measurements

Reflectance spectra were recorded with a R400-7-UV-Vis reflection probe that was coupled to an Ocean Optics S2000 fibre-coupled spectrometer and a Micropak HL-2000 halogen light source. The reflection probe was immersed in the aqueous solution and oriented 90° to the interface. The probe was positioned 1.1 mm away from the LLI, focussed onto the LLI by monitoring the signal intensity of the reflection as a function of the probe position. The spectra were recorded with a 100 ms integration time and 10 averages per acquisition. The spectra were obtained over 5 areas on the sample in order to estimate the spatial variance of the data due to local imperfections of the NP arrays. The counts were then referenced against a silver mirror which was assumed to be 100 % reflectance over the spectral range acquired.

X-ray reflectivity and grazing incidence diffraction small angle x-ray scattering measurements

Specular X-ray reflection measurements at the LLI were made using the beamline I07 at the Diamond Light Source, with a double crystal diffractometer (DCD) configuration to enable reflection from the horizontal surface. The energy of the incident beam (24 keV, λ = 0.51 Å) was chosen to maximise the penetration through the aqueous upper-phase, although this complicated the measurement of reflection at lower Q values, given the very low angles involved. The X-ray focus from the upstream mirrors was nominally ~200 – 250 mm FWHM in the vertical direction and the Pilatus 100 K detector at 0.9 m from the sample had a defined acceptance set of 17 x 5 pixels for the reflected beam which was summed, and a flat background from the same size areas subtracted close to the reflected beam. Scans were made from Q = 0.01 to 0.3 $Å^{-1}$ with a typical total exposure time of less than 2 minutes per sample. No beam damage was apparent in repeat measurements.

Grazing incidence small angle scattering measurements were made at a range of incident z - angles, with the sample to detector distance of 2.95 m, the working width of the detector of 25 cm and a height of 30 cm and with a pixel size of 172 mm. Under these conditions 50 pixels correspond to ~ 0.17°, ΔQ = 0.036 $Å^{-1}$ or a d-spacing of ~18 nm. A thin cylinder of tungsten, radius 1 mm, was placed vertically to act as a beam stop for the intense direct and specularly reflected beams. Centre-to-centre spacings (C2C) were calculated as , $C2C = \frac{2d}{\sqrt{3}}$ where d is the d -spacing.

Acknowledgements

The authors wish to thank Tom Arnold and Jonathan Rawle for assistance on the I07 beamline at Diamond light source. The authors are thankful to the EPSRC grant (EP/L02098X/1) for the support of this research. AAK also thanks EU FP7 grant Nanodetector project NMP.211.1.3-1 for partial support. JBE also acknowledges support of an ERC starting investigator grant. LV also acknowledges the support of a H2020-MSCA individual fellowship.

Notes and references

1. K. Zhang, J. Ji, Y. Li and B. Liu, *Analytical Chemistry*, 2014, **86**, 6660-6665.
2. F. Le, D. W. Brandl, Y. A. Urzhumov, H. Wang, J. Kundu, N. J. Halas, J. Aizpurua and P. Nordlander, *ACS Nano*, 2008, **2**, 707-718.
3. H. Wang, C. S. Levin and N. J. Halas, *Journal of the American Chemical Society*, 2005, **127**, 14992-14993.
4. S. Liu and Z. Tang, *Journal of Materials Chemistry*, 2010, **20**, 24-35.
5. J. F. Li, Y. F. Huang, Y. Ding, Z. L. Yang, S. B. Li, X. S. Zhou, F. R. Fan, W. Zhang, Z. Y. Zhou, Y. WuDe, B. Ren, Z. L. Wang and Z. Q. Tian, *Nature*, 2010, **464**, 392-395.
6. M. P. Cecchini, V. A. Turek, J. Paget, A. A. Kornyshev and J. B. Edel, *Nature Mater.*, 2013, **12**, 165-171.
7. J. B. Edel, A. A. Kornyshev, A. R. Kucernak and M. Urbakh, *Chemical Society Reviews*, 2016, DOI: 10.1039/C5CS00576K.
8. S. A. Maier and H. A. Atwater, *Journal of Applied Physics*, 2005, **98**, 011101.
9. C. Rockstuhl, F. Lederer, C. Etrich, T. Pertsch and T. Scharf, *Physical Review Letters*, 2007, **99**, 017401.
10. J. J. Nieminen, I. Hatay, P. Ge, M. A. Mendez, L. Murtomaki and H. H. Girault, *Chemical Communications*, 2011, **47**, 5548-5550.
11. A. N. J. Rodgers, S. G. Booth and R. A. W. Dryfe, *Electrochemistry Communications*, 2014, **47**, 17-20.
12. P. Pieranski, *Physical Review Letters*, 1980, **45**, 569-572.
13. Y. Lin, H. Skaff, T. Emrick, A. D. Dinsmore and T. P. Russell, *Science*, 2003, **299**, 226-229.
14. P. Singh, D. D. Joseph and N. Aubry, *Soft Matter*, 2010, **6**, 4310-4325.
15. F. Bresme and M. Oettel, *Journal of Physics: Condensed Matter*, 2007, **19**, 413101.
16. J. B. Edel, A. A. Kornyshev and M. Urbakh, *ACS Nano*, 2013, **7**, 9526-9532.
17. V. A. Turek, M. P. Cecchini, J. Paget, A. R. Kucernak, A. A. Kornyshev and J. B. Edel, *ACS Nano*, 2012, **6**, 7789-7799.
18. P. S. Pershan and M. L. Schlossman, *Liquid surface and interfaces: synchrotron X-ray methods*, Cambridge University Press, 2012.
19. G. Renaud, R. Lazzari and F. Leroy, *Surface Science Reports*, 2009, **64**, 255-380.
20. Y. Dai, B. Lin, M. Meron, K. Kim, B. Leahy, T. A. Witten and O. G. Shpyrko, *Langmuir*, 2013, **29**, 14050-14056.
21. K. Kim, B. D. Leahy, Y. Dai, O. Shpyrko, J. S. Soltau, M. Pelton, M. Meron and B. Lin, *Journal of Applied Physics*, 2011, **110**, 102218.
22. M. K. Bera, M. K. Sanyal, S. Pal, J. Daillant, A. Datta, G. U. Kulkarni, D. Luzet and O. Konovalov, *EPL (Europhysics Letters)*, 2007, **78**, 56003.
23. D. G. Schultz, X.-M. Lin, D. Li, J. Gebhardt, M. Meron, J. Viccaro and B. Lin, *The Journal of Physical Chemistry B*, 2006, **110**, 24522-24529.
24. S. Kubowicz, M. A. Hartmann, J. Daillant, M. K. Sanyal, V. V. Agrawal, C. Blot, O. Konovalov and H. Möhwald, *Langmuir*, 2009, **25**, 952-958.
25. M. K. Bera, H. Chan, D. F. Moyano, H. Yu, S. Tatur, D. Amoanu, W. Bu, V. M. Rotello, M. Meron, P. Král, B. Lin and M. L. Schlossman, *Nano Letters*, 2014, DOI: 10.1021/nl502450j.
26. M. K. Sanyal, V. V. Agrawal, M. K. Bera, K. P. Kalyanikutty, J. Daillant, C. Blot, S. Kubowicz, O. Konovalov and C. N. R. Rao, *The Journal of Physical Chemistry C*, 2008, **112**, 1739-1743.
27. G. Frens, *Nature*, 1973, **241**, 20-22.
28. J. Turkevich, P. C. Stevenson and J. Hillier, *Discussions of the Faraday Society*, 1951, **11**, 55-75.
29. A. V. Hughes, RasCAL. http://sourceforge.net/projects/rscl/, (accessed September 2015).
30. M. Born and E. Wolf, *Principles of Optics*, Pergamon Press: Oxford, 1970.
31. E. W. Weisstein, "Spherical Segment." From MathWorld-A Wolfram Web Resource. http://mathworld.wolfram.com/SphericalSegment.html (accessed September 2015).
32. L. Isa, F. Lucas, R. Wepf and E. Reimhult, *Nat Commun*, 2011, **2**, 438.
33. M. K. Bera, M. K. Sanyal, L. Yang, K. Biswas, A. Gibaud and C. N. R. Rao, *Physical Review B*, 2010, **81**, 115415.
34. A. L. Patterson, *Physical Review*, 1939, **56**, 978-982.
35. A. Guiner, *X-Ray Diffraction: In Crystals, Imperfect Crystals, and Amorphous Bodies*, Freeman, 1963.
36. O. Kedem, A. Vaskevich and I. Rubinstein, *The Journal of Physical Chemistry Letters*, 2011, **2**, 1223-1226.
37. P.-P. Fang, S. Chen, H. Deng, M. D. Scanlon, F. Gumy, H. J. Lee, D. Momotenko, V. Amstutz, F. Cortés-Salazar, C. M. Pereira, Z. Yang and H. H. Girault, *ACS Nano*, 2013, **7**, 9241-9248.
38. E. Smirnov, M. D. Scanlon, D. Momotenko, H. Vrubel, M. A. Méndez, P.-F. Brevet and H. H. Girault, *ACS Nano*, 2014, **8**, 9471-9481.
39. M. E. Flatté, A. A. Kornyshev and M. Urbakh, *The Journal of Physical Chemistry C*, 2010, **114**, 1735-1747.
40. A. A. Kornyshev, M. Marinescu, J. Paget and M. Urbakh, *Physical Chemistry Chemical Physics*, 2012, **14**, 1850-1859.
41. P. B. Johnson and R. W. Christy, *Physical Review B*, 1972, **6**, 4370-4379.
42. D. Sikdar, I. D. Rukhlenko, W. Cheng and M. Premaratne, *Journal of the Optical Society of America B*, 2013, **30**, 2066-2074.
43. D. Sikdar, I. D. Rukhlenko, W. Cheng and M. Premaratne, *Biomedical Optics Express*, 2013, **4**, 15-31.
44. D. Sikdar, S. B. Hasan, M. Urbakh, J. B. Edel and A. A. Kornyshev, *Physical Chemistry Chemical Physics*, 2016, **18**, 20486-20498.
45. P. K. Jain and M. A. El-Sayed, *Chemical Physics Letters*, 2010, **487**, 153-164.
46. F. M. Huang, D. Wilding, J. D. Speed, A. E. Russell, P. N. Bartlett and J. J. Baumberg, *Nano Letters*, 2011, **11**, 1221-1226.
47. P. K. Jain, W. Huang and M. A. El-Sayed, *Nano Letters*, 2007, **7**, 2080-2088.
48. K. H. Su, Q. H. Wei, X. Zhang, J. J. Mock, D. R. Smith and S. Schultz, *Nano Letters*, 2003, **3**, 1087-1090.

49. R. Aroca, *Surface-Enhanced Vibrational Spectroscopy*, John Wiley & Sons, Ltd, Chichester, UK, 2007.
50. E. C. Le Ru and P. G. Etchegoin, *Principles of Surface-Enhanced Raman Spectroscopy*, Elsevier, Amsterdam, 2009.
51. X. Liu, M. Atwater, J. Wang and Q. Huo, *Colloids and Surfaces B: Biointerfaces*, 2007, **58**, 3-7.